

Comprehensive study of solar type II radio bursts and the properties of the associated shock waves

K. Bhandari¹, D. E. Morosan^{1,2}, S. Normo¹

¹ Department of Physics and Astronomy, University of Turku, 20014 Turku, Finland
e-mail: diana.morosan@utu.fi

² Turku Collegium for Science, Medicine and Technology, University of Turku, 20014, Turku, Finland

December 29, 2025

ABSTRACT

Context. Type II radio bursts are solar radio emissions generated by electrons accelerated by coronal shocks. These bursts are typically found close to expanding coronal mass ejections (CMEs), making them valuable for studying the properties and dynamics of CME-driven shocks in the solar corona.

Aims. Here, we aim to determine the regions in the solar corona where shock waves accelerate electrons and determine their characteristic properties. To do this, we combine radio observations of type II solar radio bursts with magneto-hydrodynamic (MHD) simulations of the solar corona.

Methods. We analyse ten type II radio bursts from Solar Cycle 25 exhibiting emissions in the 150–300 MHz frequency range. The novelty of this study lies in using radio imaging data for all type II bursts to examine the positions of the radio sources. The radio source positions, combined with a geometrical fitting of the CME shock and the MHD simulations, are used to determine essential shock parameters at the acceleration region, such as the Alfvén Mach number M_A and shock normal angle relative to the magnetic field θ_{BN} . The shock parameters are then combined with the properties of the radio emission and the associated eruption in a comprehensive study.

Results. We found that for all events, the type II bursts are located near or inside coronal streamers. These streamer regions have a low Alfvén speed while the estimated shock speeds are high, resulting in the formation of super-critical shocks ($3.6 \leq M_A \leq 6.4$) at the type II locations. However, in most events, type II bursts are located at oblique shocks rather than near-perpendicular geometries, suggesting that the shock structure is more complex at local scales than the simple spherical shock models usually applied to CME shocks.

Conclusions. Our results suggest that CME-streamer interaction regions are necessary for the generation of type II bursts, as they provide ideal plasma conditions for the formation of super-critical shocks and the subsequent acceleration of electrons.

Key words. Sun: Corona - Sun: Coronal Mass Ejection (CME) - Sun: Radio radiation - Sun: Shocks in corona

1. Introduction

Solar type II radio bursts can be attributed to the propagation of collisionless shocks in the solar atmosphere, often driven by energetic eruptive events, such as coronal mass ejections (CMEs; Nelson & Melrose 1985; Mann et al. 1996). These bursts are most frequently detected in association with CMEs (Zucca et al. 2018; Mancuso et al. 2019; Morosan et al. 2020a) and in rare cases they have also been reported in connection with shocks occurring without a CME eruption (e.g. Morosan et al. 2023). Type II bursts have also been observed to be in close association with extreme ultraviolet (EUV) waves, which have been linked to large-scale fast magnetosonic MHD waves and/or shocks in the solar corona (Klassen et al. 2000; Warmuth et al. 2004; Mann et al. 2023). In the dynamic spectra, type II bursts manifest as slowly drifting features (typically $< 1 \text{ MHz s}^{-1}$), originating at higher frequencies and gradually shifting toward lower frequencies. They are emitted at both the fundamental (f_{pe}) and harmonic ($2f_{pe}$) of the plasma frequency, with the two lanes drifting almost in parallel to each other. Type II bursts are usually composed of many fine structures in a temporally well-resolved dynamic spectrum (Magdalenić et al. 2020). Among these, the ‘herringbone’ bursts appear as narrow bursts of radiation with high drift rates (for example, Fig. 2). These distinct features, that

exhibit both positive or negative drift rates in the spectrum, are often considered as signatures of individual electron beams escaping shocks (Holman & Pesses 1983; Carley et al. 2015; Mann et al. 2018). Herringbone bursts have been imaged only on rare occasions and show a close association to the CME or shock expansion in the corona (Morosan et al. 2022, 2024).

Type II bursts are generated when shock-accelerated non-thermal electrons undergo non-linear wave interactions, transferring their energy to Langmuir waves, which subsequently generate the observed radio emissions (Nelson & Melrose 1985). The sources of these bursts have been found in the upstream regions of the shocks (Bhunia et al. 2023; Normo et al. 2025). The ambient coronal conditions surrounding these sources, including the Alfvén speed (v_A) and magnetic field configuration, play a crucial role in governing the intensity of the resulting radio emissions (Mann et al. 1995; Koulooumvakos et al. 2021; Jebraj et al. 2021). Additionally, magnetic field structures such as streamer belts surrounding the source regions also influence the morphology of type II bursts, often manifesting as changes in the drift rate observed in the dynamic spectrum (Feng et al. 2013; Kong et al. 2015; Koval et al. 2023). The vicinity of coronal streamers can provide favourable conditions for type II generation, as shocks traversing regions of reduced v_A are more likely to be

come supercritical (Mancuso et al. 2019). Key shock parameters, including the Alfvén Mach number (M_A) and the angle between the magnetic field and the shock normal (θ_{BN}), govern the efficiency of electron acceleration via the shock drift acceleration (SDA) mechanism (Mann et al. 2022). The electron acceleration is more efficient for near-perpendicular shocks ($\theta_{BN} \sim 90^\circ$) that are supercritical. Therefore, it is important to study these parameters to comprehend the conditions under which shocks can efficiently generate observable type II radio emissions.

Only a limited number of studies have investigated the physical parameters of ambient plasma and the associated shocks using radio imaging of type II bursts in the solar corona (Kouloumvakos et al. 2021; Morosan et al. 2024), while others, such as Jebraj et al. (2020), have employed radio triangulation techniques to determine the source positions and properties of type II bursts in interplanetary space. We complement the ongoing studies by conducting a comprehensive investigation of multiple type II events in metric wavelengths.

In this study, we use the radio imaging observations to derive the source locations of ten type II bursts from Solar Cycle 25 and determine the ambient plasma properties around their sources. Section 2 provides an overview of the observational data and analysis methodologies employed in this study. The results are presented in Section 3 and are further discussed in Section 4.

2. Observation and Data Analysis

We conducted a comprehensive analysis of the type II bursts associated with coronal shock waves using data from various observatories and spacecraft. In total, ten type II events from Solar Cycle 25 were analysed. The events were selected based on the availability of radio imaging observations from the Nançay Radioheliograph (NRH; Kerdraon & Delouis 1997). To minimise ionospheric effects, events from the European winter months were generally excluded. However, when winter events were considered, only those occurring near local noon were selected, ensuring that the Sun was close to its maximum altitude in the sky to minimise ionospheric propagation effects. Of the events analysed in this study, eight exhibited a clear association with a CME. The remaining two events were associated with a flare and a propagating EUV wave (April 22, 2022 and March 11, 2025).

The radio spectrum data used in this study primarily come from Observations Radiospectrographiques pour FEDOME et l'Etude des Eruptions Solaires (ORFEES; Hamini et al. 2021) at frequencies of 144 – 1004 MHz and are supplemented at lower frequencies (< 144 MHz) by other observatories, such as the Nançay Decameter Array (NDA; Lecacheux 2000), the LOw Frequency ARray (LOFAR; van Haarlem et al. 2013; Zhang et al. 2022) and several e-CALLISTO stations (Benz et al. 2005) such as Landschlacht, Germany (DLR), Alexandria, HUMAIN, and DENMARK. The Stokes I images from NRH at frequencies 150, 173 and 228 MHz are used to investigate the location of the type II sources.

2.1. 2024 May 29 Type II Burst

In this subsection, we will discuss the analysis methods used in the study. To do so, we use an example event on 2024 May 29 (Fig. 1). The same methods are employed for the remaining events analysed in the study (see Appendix A.2 to A.10).

A type II radio burst was seen with an accompanying halo CME on May 29, 2024, from the southeast limb of the Sun. The event was linked to an X1.4-class flare that began at 14:11

UT with a peak at 14:37 UT. The CME in this case was observed by multiple spacecraft, such as Solar Dynamics Observatory (SDO; Pesnell et al. 2012), Solar and Heliospheric Observatory (SOHO; Domingo et al. 1995), Solar Ultraviolet Imagers (SUVI) on board the Geostationary Operational Environmental Satellite (GOES)-16 (Darnel et al. 2022), and Solar Terrestrial Relations Observatory-A (STEREO-A; Kaiser et al. 2008).

The type II burst can be seen in the composite dynamic spectrum in Fig. 1a from ORFEES, e-CALLISTO Landschlacht, and NDA. The harmonic ($2f_p$) emission of the type II burst (indicated as Type II - H in Fig. 1a) is imaged by the NRH at the following frequencies: 150, 173, and 228 MHz. The radio contours are overlaid on AIA/SDO 211Å running difference image in Fig. 1b. A 2D Gaussian function was fitted to determine the centroid location and the peak intensity of the source. The initial type II burst was followed by emissions lacking a distinct type II backbone but featuring multiple herringbone bursts (indicated as 'Herringbones' in Fig. 1a), exhibiting drifts toward both higher and lower frequencies. The herringbone drift rates were used to estimate the electron beam energy.

Combined EUV and white-light data enable a 3D reconstruction of the shock from near-simultaneous images from STEREO-A/EUVI and SDO/AIA, using a spherical model to achieve an optimal fit. EUV images from GOES/SUVI were also utilised, owing to the imager's larger field of view compared to AIA. This procedure was performed using PyThea (Kouloumvakos et al. 2022), an open-source software package for shock-wave reconstruction. The fitting was done at five different time steps between 14:26 UT and 14:36 UT, during which the shock wave was observed by both EUV instruments and white-light coronagraphs, SOHO/LASCO (Brueckner et al. 1995) and STEREO-A/COR1 (Howard et al. 2008). The angular separation between SDO and STEREO was $\sim 15^\circ$. The fitting was initially done using coronagraph images, where the CME shock is more defined, providing us with constraints on the geometry. The fitted CME model is propagated backwards in time and refined to match earlier observations from the viewpoints of SDO/AIA and STEREO-A/EUVI, ensuring an optimal fit across multiple coronal heights. This approach captures the early evolution of the CME shock while preserving consistency with its later appearance in coronagraph fields of view. The fitting parameters consist of Heliographic longitude and latitude in the Stonyhurst heliographic coordinate system, heliocentric distance of the spheroid centre r_c , radial and orthogonal axes of the spheroid, apex height, self-similar constant κ which is the ratio of one of the semi-axes to the height of the apex from the solar surface, and ϵ , which is the eccentricity of the spheroid. Table B.1 contains these parameters at different times for all the events where the CME fitting was possible. From the time evolution of the fitted parameters, for this event we estimate a shock apex speed of ~ 689 km s $^{-1}$ and a lateral expansion speed of ~ 462 km s $^{-1}$ at the time of the type II emission. Similar fittings were performed for the remaining events where the CME and shock outlines were visible in EUV or white-light images. Out of the eight CME events, only one event could not be fitted (February 08, 2024).

To determine the ambient coronal conditions associated with these radio sources, we use the Magnetohydrodynamic Algorithm outside a Sphere (MAS) model (Lionello et al. 2008) developed by Predictive Science Inc¹. The MAS is an MHD model that uses photospheric magnetic field data, obtained from SDO/Helioseismic and Magnetic Imager (HMI; Scherrer et al.

¹ www.predsci.com

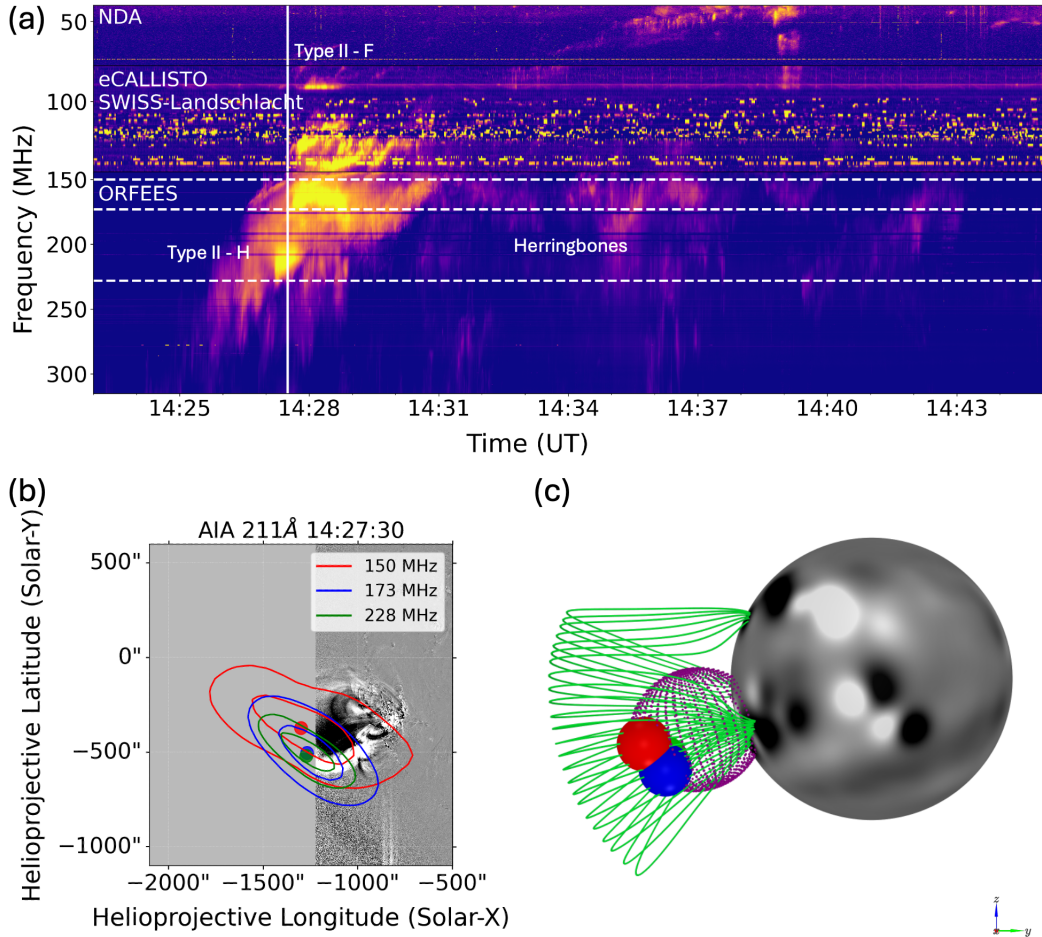


Fig. 1: Composite dynamic spectrum and radio source locations from 29 May 2024. Panel a: Low-frequency dynamic spectrum (315–40 MHz) combines NDA, e-CALLISTO Landschlacht, and ORFEES data. Horizontal dashed lines mark the NRH imaging frequencies used for panel b at the time indicated by the vertical dashed line. Panel b: Type II radio source contours are shown on an AIA 211Å running-difference image of the associated CME eruption. Contours mark different frequencies—150 MHz (red), 173 MHz (blue), 228 MHz (green)—matching dashed horizontal lines in panel a, and are drawn at 40% and 80% of maximum intensity. Panel c: De-projected radio source positions from panel b are plotted on the photospheric magnetogram, along with closed field lines (green) near the sources (viewed from Earth, x-axis toward Earth). The reconstructed CME shock at 14:26 UT appears as a magenta mesh.

2012) as the boundary condition at the solar surface. The synoptic magnetograms used in the model are constructed by continuously updating the magnetic field measurements along the central meridian of the Sun, thereby producing a full-Sun magnetic map. This can introduce additional uncertainties, as the magnetogram may be outdated and not representative of the magnetic field configuration at the time of the event. However, special care was taken to make sure the simulation magnetogram used for the modelling closely matched the magnetogram at the time of the observations. We use the model results to estimate coronal properties, such as electron density and magnetic field, which are then used to determine the global Alfvén (v_A) and fast magnetosonic speeds (v_{FMS}). The coronal densities are scaled up by a factor of 2 for better agreement with observations (Wang et al. 2017).

The electron densities are used to deproject the plane-of-sky radio centroids determined from the NRH images (see, for example, the methods of Morosan et al. 2022). We compute the

electron density surface corresponding to the plasma frequency (f_{pe}) of 150 MHz. Overlaid on this surface, we include the de-projected type II centroid as shown in Fig. 3. The density surface is overlaid with the Alfvén speed (v_A) values obtained previously. Additionally, the shock geometry is assessed by deriving the angle between the magnetic field (\mathbf{B}) and the shock normal ($\hat{\mathbf{n}}$), denoted as θ_{BN} . In Fig. 4, the shock geometry is outlined, where the reconstructed shock is plotted along with the photospheric magnetic field, along with closed (green) and open (black) magnetic field lines. The shock surface is overlaid with the θ_{BN} angle.

The herringbone bursts are analysed to estimate the speeds of the electron beams escaping from the shock (Fig. 2a). Here, we use the radio images to determine the speeds of the herringbone radio sources. The images can only be used for this purpose when these fine structures in the spectrum intersect at least two NRH imaging frequencies (for example, Fig. 2a). When this is not the case, we instead use a four-fold Newkirk density model

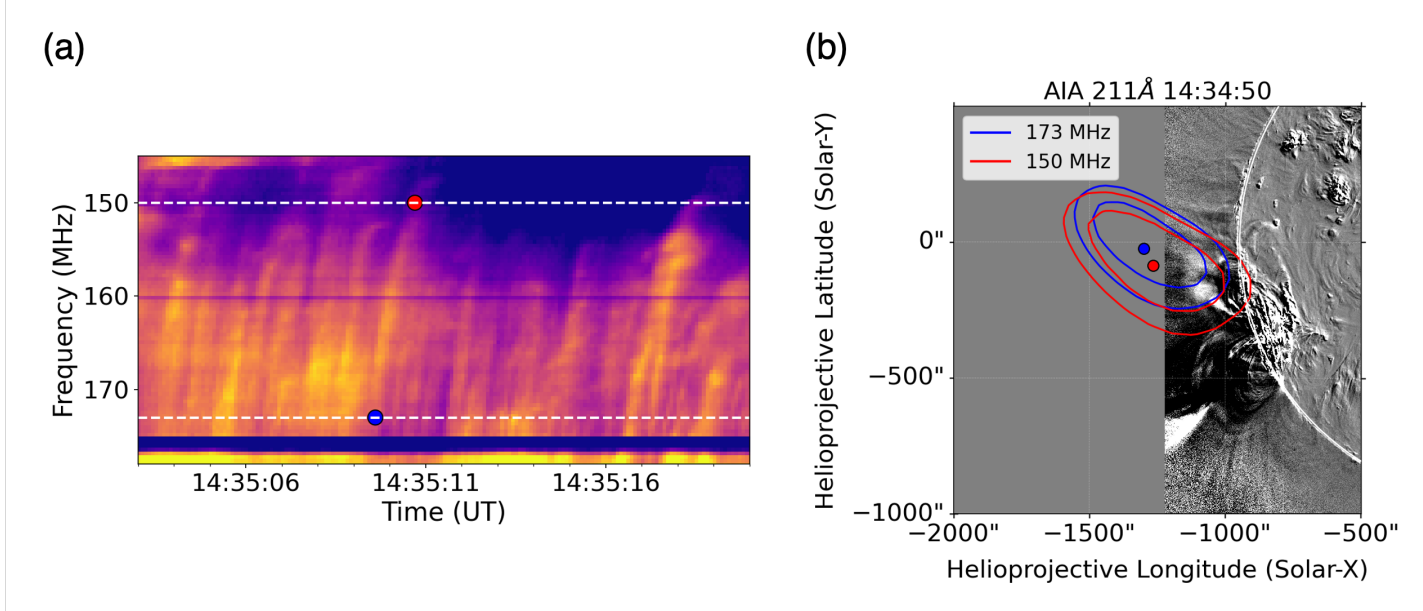


Fig. 2: Herringbone burst. Panel a: Zoomed-in dynamic spectrum showing the herringbone structures, at 173 MHz (blue) and 150 MHz (red). The dashed horizontal lines represent the two imaging frequencies used. Panel b: AIA running difference image overlaid with NRH contours at 40% and 80% of the maximum value.

Table 1: Results of the study, including CME speeds derived from CME fitting and LASCO catalogue, shock parameters such as θ_{BN} angle, Alfvén (M_A) and Fast Magnetosonic (M_{FMS}) Mach number, and electron beam energies obtained from the herringbone observations.

Date	Shock Apex speed (km/s)	Shock Lateral speed (km/s)	LASCO catalogue speed (km/s)	Type II duration (mins)	Type II frequency range (MHz)	GOES flare class	Electron beam energy (keV)	θ_{BN} (°)	Alfvén Mach number M_A	Fast magnetosonic Mach number M_{FMS}
2021/06/09	699	487	282	19	475-20	C1.7*	588, D	40-50	6.1	2.8
2022/03/28	897	637	312	14	240-20	M4.1	11, I	60-80	6.4	4.5
2022/04/22	–	–	–	6	290-60	M3.4	24, D	–	–	–
2022/05/19	1044	710	277	23	640-40	X1.4†	145, I	40-50	3.6	2.3
2022/11/19	566	401	276	20	240-20	M1.6	12, I	20-30	4.1	2.5
2024/02/08	–	–	–	9	280-40	C9.8	9, I	–	–	–
2024/03/10	1100	965	339	15	230-40	M7.4	19, I	50-60	5.7	3.4
2024/05/29	681	561	583	15	295-30	X1.4	13, I	70-90	3.5	3.1
2024/11/10	900	589	325	24	250-7	M9.5	6, D	50-60	4.5	3.5
2025/03/11	–	–	–	8	650-50	M1.1	4, I	–	–	–

Note: * denotes the far-side flare event that was partially observed by GOES. † denotes the far-side event with the GOES flare class estimated by STIX/SoLO. Column 7: Electron energy estimates along with the technique used; I = using images; D = using density model.

(Newkirk 1961) – that provides the coronal densities at various heights – to estimate the speed of the electron beams from their drift rate in the spectrum. The radio images closely matching the timing for the respective frequency are chosen. The plane-of-sky distance between the radio centroids, along with the time interval between them, helps to determine the lower limit for the speed of the herringbone sources. The speeds derived from the radio images are also compared with those calculated from the density model. From the density model, we get an estimate for the speed of the electron beam of $0.12 c$. On the other hand, the

analysis of the herringbone source in the images at 173 and 150 MHz, shown in Fig. 2b, gives us a speed of $0.22 c$. This speed corresponds to an electron beam energy of 13.07 keV . Similar methods were then employed for the remaining events as well.

3. Results

In this section, we present our findings and common properties of the type II bursts and those of the shock at the acceleration regions:

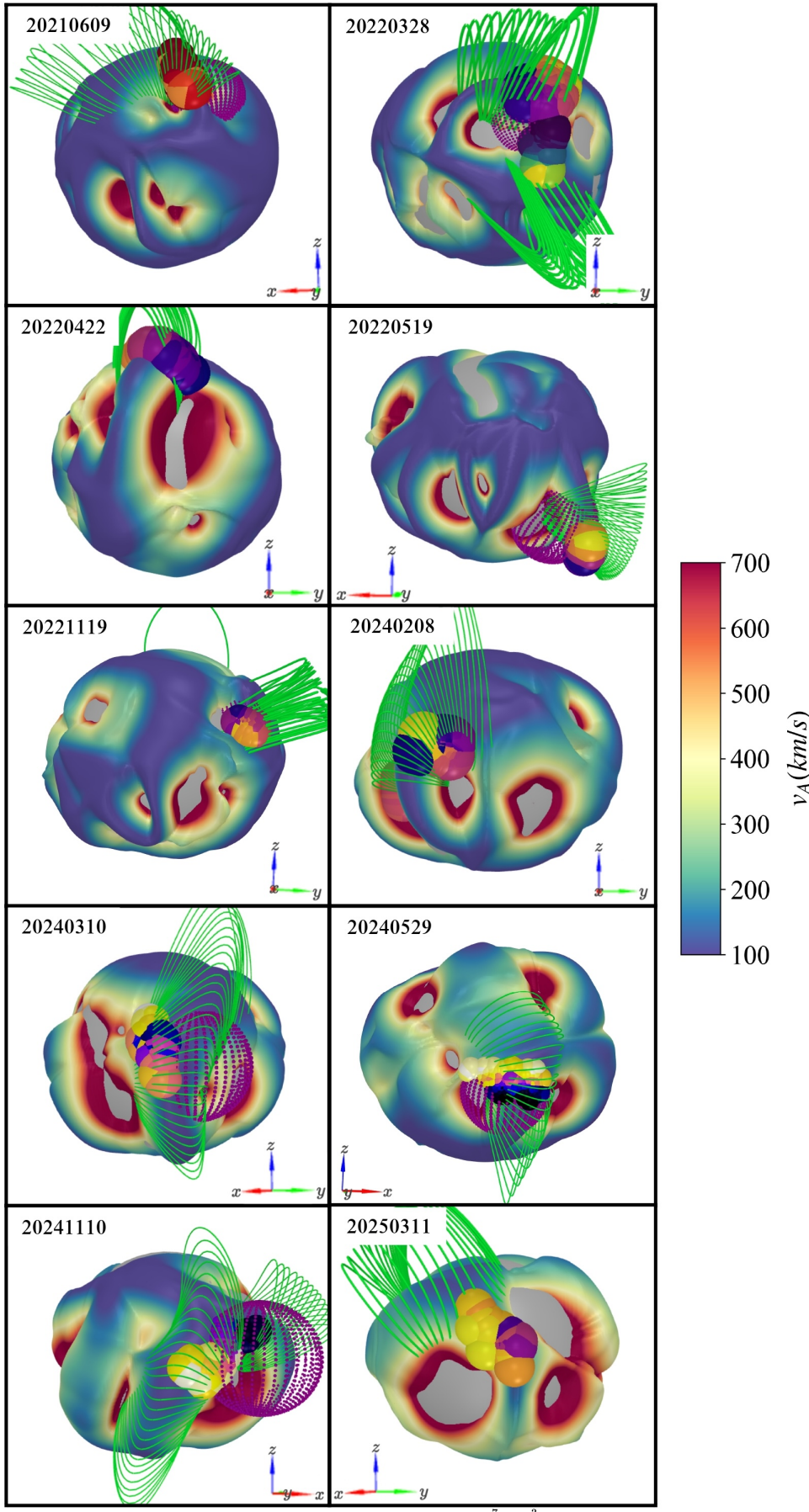


Fig. 3: Density isosurface corresponding to the plasma frequency of 150 MHz harmonic emission, overlaid with Alfvén speed (v_A) values. Grey spheres of radius $1.2 R_\odot$ provide a visual reference for the height of the density isosurface. De-projected radio sources (coloured spheres), shock reconstruction (magenta wire mesh), and closed magnetic field lines (green) are overlaid on the density isosurface. The coordinate axis on the bottom left indicates the orientation of the Sun with the x-axis pointing toward Earth.

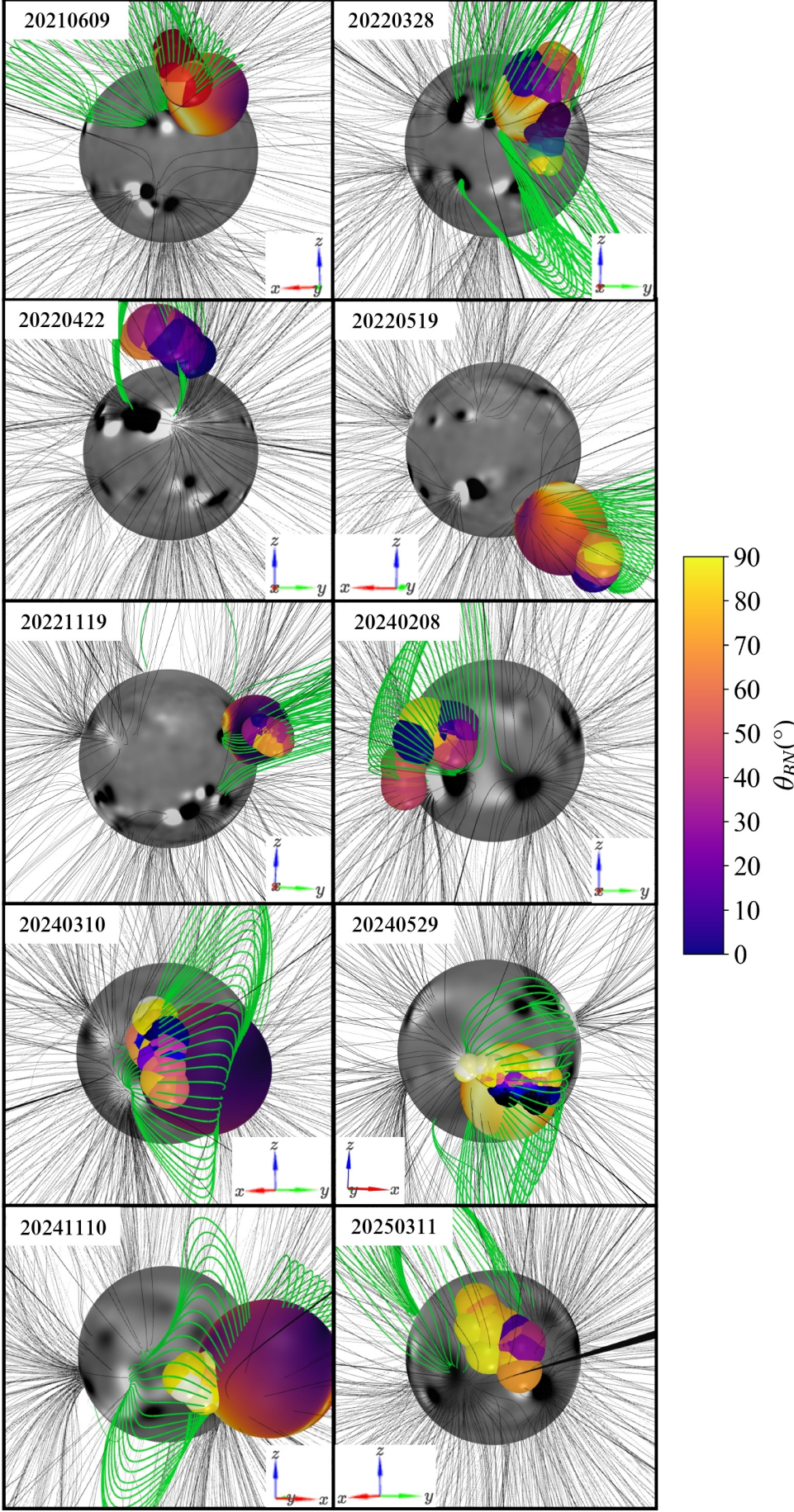


Fig. 4: Shock reconstruction in 3D (when visible) for all ten events included in the study. The reconstruction is timed to coincide with the onset of the type II radio burst or the earliest instance at which the shock reconstruction was possible. The time of the shock reconstruction for all the events is indicated as a solid vertical line in their respective spectrums in Fig. 1 and A.2 - A.10. The shock reconstruction is overlaid with θ_{BN} values, along with the de-projected radio sources (coloured spheres) obtained from Gaussian fitting analysis (see Section 1). Photospheric magnetogram overlaid with both open (black) and closed (green) magnetic field lines from MAS simulation. The coordinate axis on the bottom left indicates the orientation of the Sun with the x-axis pointing toward Earth.

To determine the type II location relative to the shock, a spherical fitting for the shocks was performed for 7 out of 10 bursts, as they had an associated CME that was well-observed remotely and from multiple viewpoints. Whereas, for the remaining three events, geometric fitting was not performed for the following reasons: the type II burst on February 8, 2022, was associated with a CME moving on the disc in the North direction when observed from Earth, making it difficult to fit a spherical model. During the events on April 22, 2022, and March 11, 2025, no CME was recorded. The shock was fitted at different times, which allows us to evaluate its evolution and shock speed at various times. The apex and lateral shock speed derived from the fits are reported in Table 1. The shock speeds associated with these events are all fast, with apex speeds exceeding 500 km/s and lateral speeds also over 400 km/s in the low corona.

The flare classes corresponding to the type II bursts are reported in Table 1. For events originating on the visible side of the Sun, all associated flares were relatively strong, with classes of at least C9.8. However, for far-side events (such as June 9, 2021 and May 19, 2022), the reported GOES flare classes may not accurately represent their true magnitudes. In particular, the May 19, 2022 flare, observed by the Spectrometer/Telescope for Imaging X-rays (STIX) onboard Solar Orbiter, was estimated to correspond to a GOES flare class of $X1.9^{+X2.8}_{-M7.7}$. The event on June 9, 2021, also occurred on the far side of the Sun and was partially observed by the GOES satellite. The type II durations are also reported in the table, and we obtain a range of 6 – 23 minutes. Two events with the shortest emission times (April 22, 2022, and March 11, 2025) did not have an associated CME. The remaining events with longer durations were all associated with a CME.

The electron beam energies are determined by analysing the herringbone structures observed in each event. Radio images were used to determine the locations of the herringbone sources at various imaging frequencies corresponding to the herringbone features seen in the dynamic spectrum. The electron beam speed is estimated from plane-of-sky radio images, and in cases where projection effects are significant, this speed provides a lower limit for the electron energies. The estimates of the energies of the electron beams are reported in the Table 1. We obtain a range of 6 – 588 keV for the electron beam energy, with most values being $\lesssim 25$ keV (i.e. $\lesssim 0.3$ c). The electron speeds derived in our study are consistent with previous herringbone analyses, with reported averages ranging from 0.14 c to 0.18 c (Mann & Klassen 2005; Carley et al. 2015; Mann et al. 2018; Morosan et al. 2024). However, electron beam energies exceeding 100 keV were found in two events, with one as high as 588 keV. Such high beam energies have only been found before in the study of Zhang et al. (2024), which proposed a specific scenario contributing to their generation, coming from counter-streaming electrons.

The plane-of-sky radio source positions at 150 MHz are de-projected using the corresponding density surface at the plasma emission frequency, provided by the MAS model. Fig. 3 shows the layer of the solar corona with an electron density corresponding to the harmonic plasma emission at $f_{pe} = 150$ MHz (i.e. $n_e = 6.977 \times 10^7 \text{ cm}^{-3}$), as all the type II imaged here are predominantly harmonic emissions. The density surface is overlaid with Alfvén speed values obtained from the MAS electron densities and magnetic field strength. Also depicted in these panels are the closed (green) magnetic field lines obtained from the model stretching up to a height of $\sim 2R_\odot$. The closed field lines in the region around the type II radio sources are shown. The panels of Fig. 3 show that the radio sources are located in the regions with low Alfvén speed ($v_A \lesssim 200$ km/s) and also inside or next to the

closed field regions. In these regions, a shock is more likely to become supercritical when it is driven by a suitably fast CME. A supercritical shock is required for the generation of the type II burst, which means the shock speed should exceed the Alfvén speed (Kouloumvakos et al. 2021). Based on the location of the radio sources with respect to the shock, either the apex or lateral speed was used for estimating the Alfvén Mach number by taking the ratio of shock speed to the local Alfvén speed. We obtain Alfvén Mach numbers spanning the range $3.6 < M_A < 6.4$, indicating the presence of supercritical shocks in all events. We also estimate the fast magnetosonic Mach number for the events and found them to be in the range $2.3 < M_{FMS} < 4.5$. The estimated M_A and M_{FMS} values for seven of the events are reported in Table 1.

The magnetic field values in the solar corona are provided by the MAS model, which allows us to evaluate the magnetic field configuration around the type II sources. In Figures 3 and 4, the closed magnetic field lines (green) in the vicinity of the type II sources are shown. These closed magnetic field regions are the low corona counterpart of a streamer and are characterised by higher plasma density than their surroundings, resulting in the formation of regions with lower Alfvén speed. In Figures 3 and 4, we note that the type II radio sources in all the events lie within or in proximity to these streamers. This suggests that shock-streamer interactions play a key role in accelerating electrons and the subsequent generation of type II bursts. These findings align with previous studies suggesting that streamer structures can act as efficient sites for electron acceleration (Kong et al. 2015).

The geometry of shocks associated with the type II bursts is identified by determining the angle between the shock normal (\hat{n}) and the magnetic field (\mathbf{B}), denoted as θ_{BN} . Fig. 4 consists of the photospheric magnetogram overlaid with open (black) and closed (green) magnetic field lines. To depict the θ_{BN} angles at the shock, the figure also consists of the reconstructed shock surface overlaid with the θ_{BN} value. The range of values corresponding to the type II locations is reported in Table 1. The derived θ_{BN} angles consistently indicate the presence of globally oblique shocks at the location of type II bursts, with the values being mostly $< 80^\circ$. The presence of a near-perpendicular shock is, however, expected for the acceleration of type II burst generating electrons (Mann et al. 1995).

4. Discussions

A comprehensive analysis of ten type II bursts was conducted to determine the ambient plasma parameters at their locations and the associated shock properties. These events were accompanied by strong flares and fast CMEs, except for two that did not have an accompanying CME. This combined study of multiple type II radio bursts reveals the following main findings that are common to all of these separate events:

- The type II sources identified in this study are all located in regions of low Alfvén speed. To quantify the strength of the associated shocks, we derived the Alfvén Mach number M_A for events where the shock fitting was possible. The critical magnetosonic Mach number (M_{FMS}^*), which determines whether a shock is supercritical or subcritical, depends primarily on θ_{BN} for $\beta_{\text{plasma}} \ll 1$ (i.e., when the plasma pressure is much lower than the magnetic pressure). Edmiston & Kennel (1984) reported that the critical magnetosonic Mach number M_{FMS}^* depends on the shock geometry, varying from about 2.76 in the quasi-perpendicular limit to about 1.53 for

quasi-parallel shocks. Additionally, [Mann et al. \(2022\)](#) found that, for plasma conditions at the 25 MHz plasma frequency level, Langmuir waves are efficiently generated by electrons accelerated by coronal shocks with Alfvén Mach numbers in the range $1.59 < M_A < 2.53$. Other observational studies, such as [Bemporad & Mancuso \(2011\)](#); [Kouloumvakos et al. \(2021\)](#), have shown that the onset of type II emission closely coincides with the transition from a subcritical to a supercritical shock. The Mach numbers determined in our study are in the range $3.6 < M_A < 6.4$ and $2.3 < M_{FMS} < 4.5$. These results indicate that the shocks analysed here are predominantly supercritical, and therefore capable of efficiently accelerating electrons.

- The analysis of the magnetic field configuration produced by the MAS model shows that all type II sources identified in this study lie inside or adjacent to the closed magnetic loops that constitute the low-coronal counterparts of streamers. These streamers separate regions of opposite magnetic polarity and contain enhanced-density plasma, leading to lower Alfvén speeds where shocks can become supercritical, as discussed earlier. Previous studies ([Mancuso & Raymond 2004](#); [Cho et al. 2008](#); [Jebaraj et al. 2020, 2021](#); [Kouloumvakos et al. 2021](#); [Koval et al. 2023](#)) have proposed that type II bursts are generated when a CME-driven shock propagates within or in proximity to streamer regions. Simulations of coronal shocks interacting with streamers have further shown that such regions can efficiently accelerate particles to energies exceeding 100 MeV, facilitated by the quasi-perpendicular shock geometry and the trapping effects created by the closed magnetic field structures ([Kong et al. 2019](#)). These simulation results are consistent with the observations of [Frassati et al. \(2022\)](#), who reported high-energy (~ 100 MeV) particles during shock propagation through streamer-like regions, reinforcing the idea that streamers provide favourable conditions for efficient electron acceleration. Our results, therefore, align closely with previous observational and simulation studies. The localisation of type II sources within low-Alfvén speed streamer structures, the likelihood of supercritical shock formation, and the associated favourable shock geometry are all consistent with the shock-streamer interaction scenario proposed in earlier works.
- The shock geometry around the type II sources shows that most events are associated with globally oblique shocks, with θ_{BN} values typically below $\sim 80^\circ$. A near-perpendicular shock geometry is required for the acceleration of electrons via the SDA mechanism ([Mann et al. 2018](#)), and consequently, the generation of type II bursts ([Kouloumvakos et al. 2021](#)). Our findings suggest that global shock reconstructions, such as spherical or spheroidal shock fits, may not reliably capture the local geometry at the type II source regions. An explanation for the presence of an oblique shock instead of a quasi-perpendicular shock can be found in the Discussion section of [Morosan et al. \(2024\)](#), where the authors consider two possible scenarios. In the first, the shock front is intrinsically non-planar, such as wavy or rippled, leading to local shock geometry alternating between quasi-parallel and quasi-perpendicular. This allows certain patches of an otherwise oblique or parallel shock to become locally quasi-perpendicular and capable of producing type II emission. Such non-planar structures can also enable electrons to encounter the shock multiple times, gaining energy at each crossing ([Zlobec et al. 1993](#); [Morosan et al. 2020b](#)). The second scenario involves non-ideal magnetic fields with

strong, large-amplitude fluctuations. These magnetic inhomogeneities can create locally perpendicular configurations even within globally parallel shocks, and have been proposed in earlier studies to explain herringbone structures ([Mann & Classen 1995](#)). The systematically low θ_{BN} values in our events point towards the presence of such non-ideal or locally structured shock and magnetic field configurations.

Our study highlights the coronal conditions common to the ten observed type II bursts. The use of radio imaging data for the study provides accurate spatial positions for the type II sources in the solar corona, enabling the determination of ambient plasma parameters around the shock. The shared features, such as low Alfvén speeds and locations inside or near streamers, suggest that these regions provide favourable conditions for shock formation and radio emission.

In future studies, it will be important to investigate the accelerated particles in type II events and their solar energetic particle (SEP) counterparts in in situ measurements. The connection between these shock-accelerated electrons and those measured in situ remains poorly understood. In-situ measurements connected to radio bursts positions in the low corona have only been done on a few occasions (e.g. [Morosan et al. 2024](#)).

Acknowledgements. K.S.B., D.E.M., and S.N. acknowledge the Research Council of Finland project 'SolShocks' (grant number 354409). S.N. acknowledges the Vilho, Yrjö and Kalle Viäsälä Foundation of the Finnish Academy of Science and Letters. This study has received funding from the European Union's Horizon Europe research and innovation programme under grant agreement No. 101134999 (SOLER). We thank the Radio Solar Database service at LESIA & USN (Observatoire de Paris) for making the NRH/ORFEES/NDA data available. We also thank the eCALLISTO network and the LOFAR IDOLS project for the availability of radio spectra. K.S.B. acknowledges helpful comments and suggestions from Rami Vainio, which helped to improve the presentation of the results.

References

- Bemporad, A. & Mancuso, S. 2011, *The Astrophysical Journal*, 739, L64, publisher: IOP ADS Bibcode: 2011ApJ...739L..64B
- Benz, A. O., Monstein, C., & Meyer, H. 2005, *Solar Physics*, 226, 143, arXiv:astro-ph/0410437
- Bhunia, S., Carley, E. P., Oberoi, D., & Gallagher, P. T. 2023, *Astronomy & Astrophysics*, 670, A169
- Brueckner, G. E., Howard, R. A., Koomen, M. J., et al. 1995, *Solar Physics*, 162, 357
- Carley, E. P., Reid, H., Vilmer, N., & Gallagher, P. T. 2015, *Astronomy and Astrophysics*, 581, A100, aDS Bibcode: 2015A&A...581A.100C
- Cho, K. S., Bong, S. C., Kim, Y. H., et al. 2008, *Astronomy and Astrophysics*, 491, 873, publisher: EDP ADS Bibcode: 2008A&A...491..873C
- Darnel, J. M., Seaton, D. B., Bethge, C., et al. 2022, *Space Weather*, 20, e2022SW003044, eprint: <https://agupubs.onlinelibrary.wiley.com/doi/pdf/10.1029/2022SW003044>
- Domingo, V., Fleck, B., & Poland, A. I. 1995, *Solar Physics*, 162, 1, aDS Bibcode: 1995SoPh..162....1D
- Edmiston, J. P. & Kennel, C. F. 1984, *Journal of Plasma Physics*, 32, 429
- Feng, S. W., Chen, Y., Kong, X. L., et al. 2013, *The Astrophysical Journal*, 767, 29, publisher: The American Astronomical Society
- Frassati, F., Laurenza, M., Bemporad, A., et al. 2022, *The Astrophysical Journal*, 926, 227, publisher: The American Astronomical Society
- Hamini, A., Auxepaules, G., Birée, L., et al. 2021, *Journal of Space Weather and Space Climate*, 11, 57
- Howard, R. A., Moses, J. D., Vourlidas, A., et al. 2008, *Space Science Reviews*, 136, 67
- Jebaraj, I. C., Kouloumvakos, A., Magdalenić, J., et al. 2021, *Astronomy & Astrophysics*, 654, A64
- Jebaraj, I. C., Magdalenić, J., Podladchikova, T., et al. 2020, *Astronomy and Astrophysics*, 639, A56, aDS Bibcode: 2020A&A...639A..56J
- Kaiser, M. L., Kucera, T. A., Davila, J. M., et al. 2008, *Space Science Reviews*, 136, 5

Kerdraon, A. & Delouis, J.-M. 1997, in *Coronal Physics from Radio and Space Observations*, Vol. 483, 192, aDS Bibcode: 1997LNP..483..192K

Klassen, A., Aurass, H., Mann, G., & Thompson, B. J. 2000, *Astronomy and Astrophysics Supplement Series*, 141, 357, publisher: EDP ADS Bibcode: 2000A&AS..141..357K

Kong, X., Chen, Y., Guo, F., et al. 2015, *The Astrophysical Journal*, 798, 81, aDS Bibcode: 2015ApJ...798...81K

Kong, X., Guo, F., Chen, Y., & Giacalone, J. 2019, *The Astrophysical Journal*, 883, 49, publisher: IOP ADS Bibcode: 2019ApJ...883...49K

Kouloumvakos, A., Rodríguez-García, L., Gieseler, J., et al. 2022, *Frontiers in Astronomy and Space Sciences*, 9, publisher: Frontiers

Kouloumvakos, A., Rouillard, A., Warmuth, A., et al. 2021, *The Astrophysical Journal*, 913, 99, publisher: IOP ADS Bibcode: 2021ApJ...913..99K

Koval, A., Stanislavsky, A., Karlický, M., et al. 2023, *The Astrophysical Journal*, 952, 51, publisher: The American Astronomical Society

Lecacheux, A. 2000, *Geophysical Monograph Series*, 119, 321, aDS Bibcode: 2000GMS..119..321L

Lionello, R., Linker, J. A., & Mikić, Z. 2008, *The Astrophysical Journal*, 690, 902, publisher: The American Astronomical Society

Magdalenić, J., Marqué, C., Fallows, R. A., et al. 2020, *The Astrophysical Journal Letters*, 897, L15

Mancuso, S., Frassati, F., Bemporad, A., & Barghini, D. 2019, *Astronomy & Astrophysics*, 624, L2

Mancuso, S. & Raymond, J. C. 2004, *Astronomy and Astrophysics*, 413, 363, aDS Bibcode: 2004A&A..413..363M

Mann, G. & Classen, H. T. 1995, *Astronomy and Astrophysics*, 304, 576, aDS Bibcode: 1995A&A..304..576M

Mann, G., Classen, T., & Aurass, H. 1995, *Astronomy and Astrophysics*, 295, 775, aDS Bibcode: 1995A&A..295..775M

Mann, G. & Klassen, A. 2005, *Astronomy & Astrophysics*, 441, 319

Mann, G., Klassen, A., Classen, H.-T., et al. 1996, *Astronomy and Astrophysics Supplement Series*, 119, 489

Mann, G., Melnik, V. N., Rucker, H. O., Konovalenko, A. A., & Brazhenko, A. I. 2018, *Astronomy and Astrophysics*, 609, A41, aDS Bibcode: 2018A&A..609A..41M

Mann, G., Vocks, C., Warmuth, A., et al. 2022, *Astronomy & Astrophysics*, 660, A71

Mann, G., Warmuth, A., & Önel, H. 2023, *Astronomy & Astrophysics*, 675, A129

Morosan, D. E., Palmerio, E., Lynch, B. J., & Kilpua, E. K. J. 2020a, *Astronomy and Astrophysics*, 633, A141, publisher: EDP ADS Bibcode: 2020A&A..633A.141M

Morosan, D. E., Palmerio, E., Räsänen, J. E., et al. 2020b, *Astronomy & Astrophysics*, 642, A151

Morosan, D. E., Pomoell, J., Kumari, A., Kilpua, E. K. J., & Vainio, R. 2023, *Astronomy and Astrophysics*, 675, A98, publisher: EDP ADS Bibcode: 2023A&A..675A..98M

Morosan, D. E., Pomoell, J., Kumari, A., Vainio, R., & Kilpua, E. K. J. 2022, *Astronomy & Astrophysics*, 668, A15

Morosan, D. E., Pomoell, J., Palmroos, C., et al. 2024, *Astronomy & Astrophysics*, 683, A31

Nelson, G. J. & Melrose, D. B. 1985, in *Solar Radiophysics: Studies of Emission from the Sun at Metre Wavelengths*, 333–359, aDS Bibcode: 1985srph.book..333N

Newkirk Jr., G. 1961, *The Astrophysical Journal*, 133, 983, publisher: IOP ADS Bibcode: 1961ApJ...133.983N

Normo, S., Morosan, D. E., Zhang, P., Zucca, P., & Vainio, R. 2025, *Astronomy & Astrophysics*, 698, A175, publisher: EDP Sciences

Pesnell, W. D., Thompson, B. J., & Chamberlin, P. C. 2012, *Solar Physics*, 275, 3, aDS Bibcode: 2012SoPh..275....3P

Scherrer, P. H., Schou, J., Bush, R. I., et al. 2012, *Solar Physics*, 275, 207, aDS Bibcode: 2012SoPh..275..207S

van Haarlem, M. P., Wise, M. W., Gunst, A. W., et al. 2013, *Astronomy and Astrophysics*, 556, A2, publisher: EDP ADS Bibcode: 2013A&A..556A..2V

Wang, T., Reginald, N. L., Davila, J. M., St. Cyr, O. C., & Thompson, W. T. 2017, *Solar Physics*, 292, 97

Warmuth, A., Vršnak, B., Magdalenić, J., Hanslmeier, A., & Otruba, W. 2004, *Astronomy & Astrophysics*, 418, 1117

Zhang, P., Morosan, D., Kumari, A., & Kilpua, E. 2024, *Astronomy & Astrophysics*, 683, A123

Zhang, P., Zucca, P., Kozarev, K. A., Gallagher, P., & Nedal, M. 2022, in *Proceedings of AGU Fall Meeting (AGU)*

Zlobec, P., Messerotti, M., Karlický, M., & Urbarz, H. 1993, *Solar Physics*, 144, 373, aDS Bibcode: 1993SoPh..144..373Z

Zucca, P., Morosan, D., Rouillard, A., et al. 2018, *Shock location and CME 3-D reconstruction of a solar type II radio burst with LOFAR*

Appendix A: Observations of the type II events analysed for the study

The radio observations, including dynamic spectra and radio intensity contours at 150, 173, and 228 MHz, are presented below for each event analysed in this study. Figures A.2 to A.10 show composite dynamic spectra obtained from ORFEES, NDA, LOFAR-IDOLS, and e-CALLISTO observatories. Below each dynamic spectrum, a second figure (bottom left) is overlaid on running-difference SDO/AIA 211Å images that closely match the corresponding radio images. The time corresponding to each image is marked on the dynamic spectrum with a white vertical line, while the dashed horizontal lines indicate the NRH imaging frequencies used. The third figure (bottom right) represents the solar magnetogram at the time of the event, which serves as the boundary condition for the MAS model. This figure also includes closed magnetic field lines (green) extending up to a height of $\sim 2R_\odot$, while the magenta mesh represents the reconstructed shock. The centroids derived from the radio images are de-projected using the global density information from the MAS model and plotted on this diagram.

Fig. A.1: Date: 2021/06/09

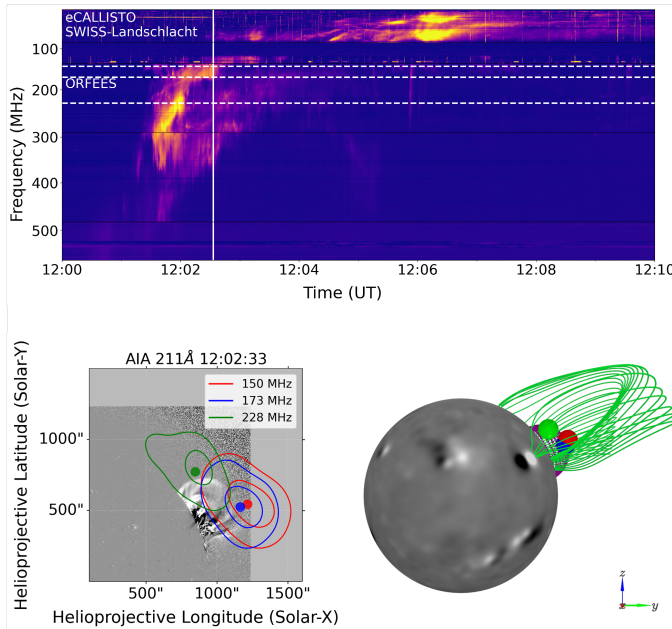


Fig. A.2: Observations of the rest of the events. Top: Composite dynamic spectrum comprising the observations from ORFEES, eCALLISTO. Horizontal dashed lines denote the imaging frequencies (i.e. 150, 173 and 228 MHz). Bottom left: SDO/AIA running difference images at 211Å overlaid with 40% and 80% contours of NRH images along with the respective centroids, at the frequencies marked in the spectrum. Bottom right: De-projected radio sources from the bottom right panel, plotted on the photospheric magnetogram, along with the closed magnetic field lines (green) near the sources (as viewed from the Earth, x-axis toward Earth). The reconstructed CME shock (magenta mesh) at the closest available time to the type II onset at the above frequencies

Fig. A.3: Date: 2022/03/28

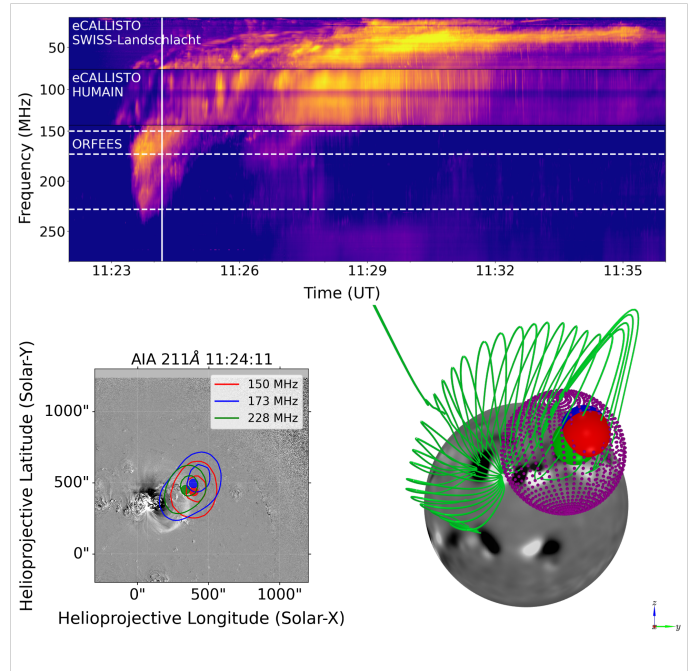


Fig. A.4: Date: 2022/04/22

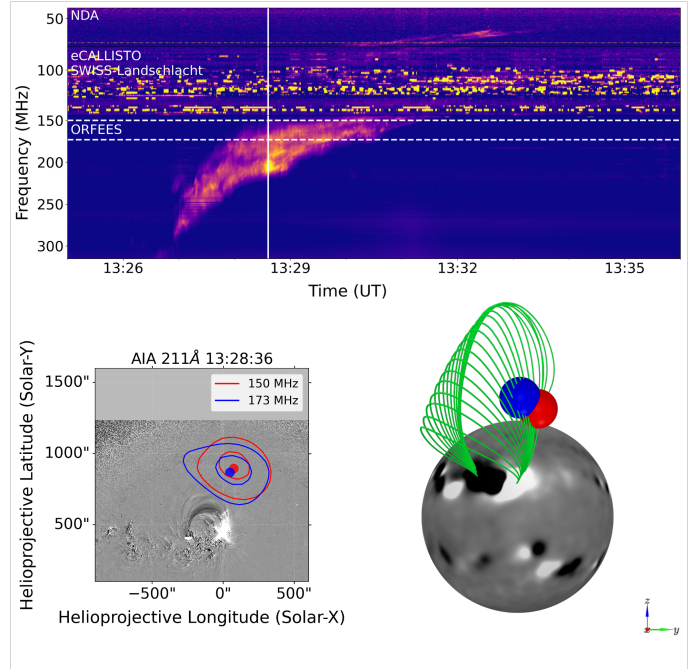


Fig. A.5: Date: 2022/05/19

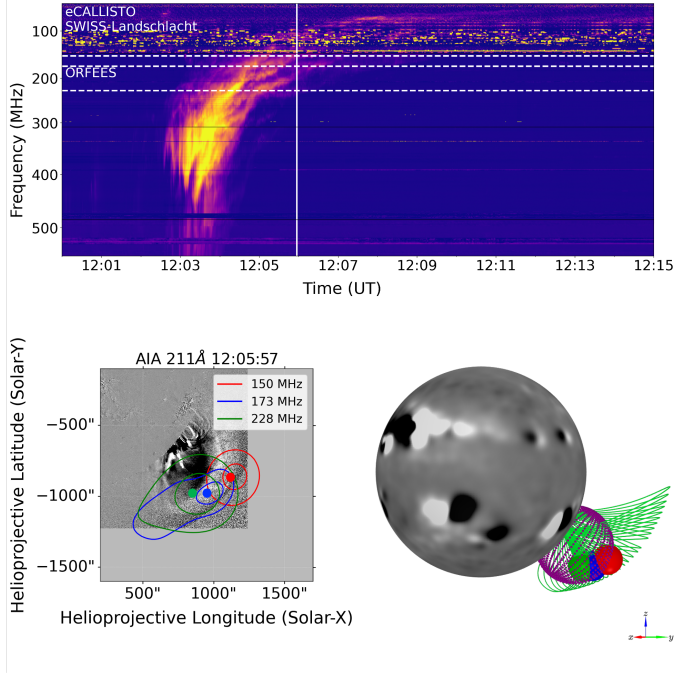


Fig. A.7: Date: 2024/02/08

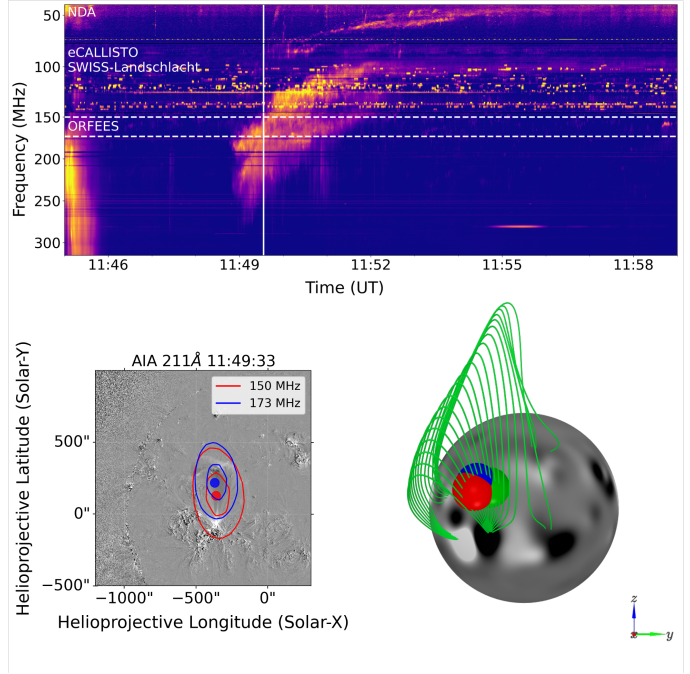


Fig. A.6: Date: 2022/11/19

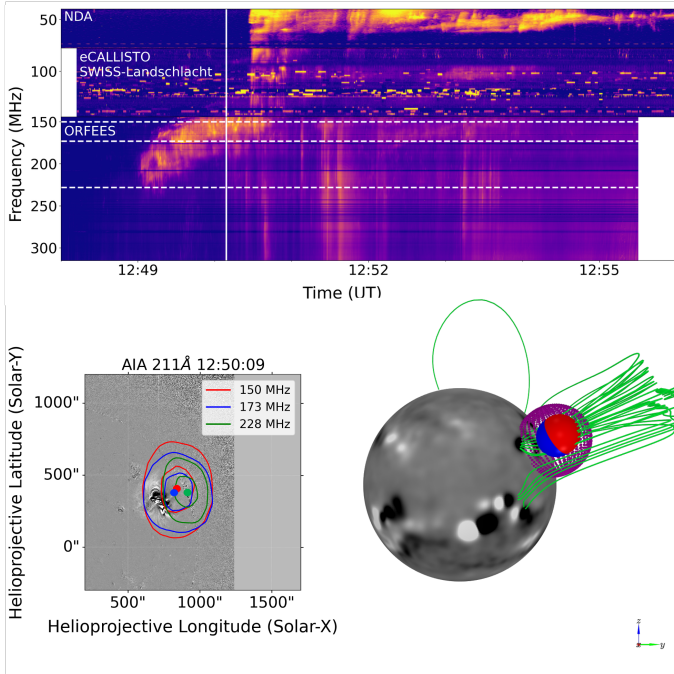


Fig. A.8: Date: 2024/03/10

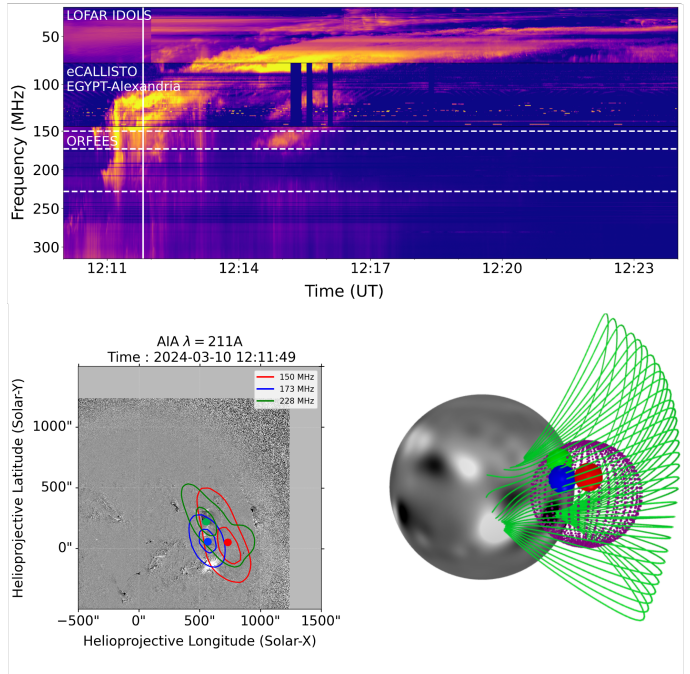


Fig. A.9: Date: 2024/11/10

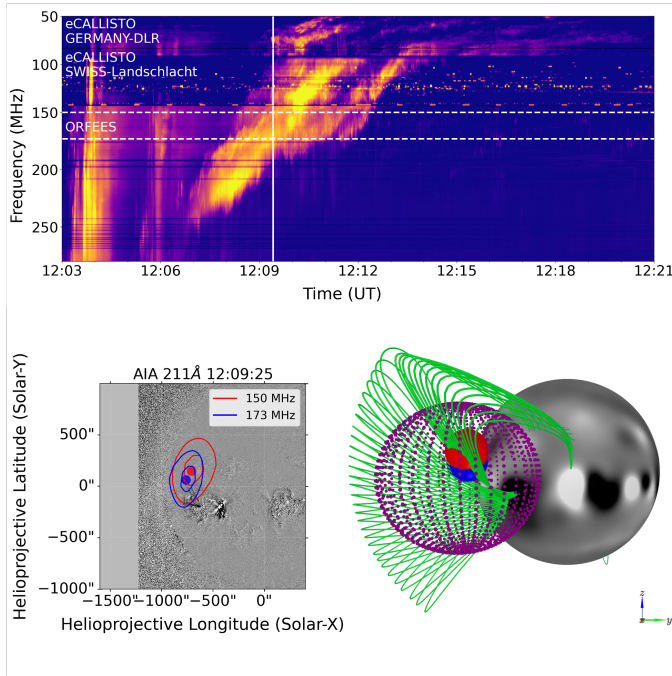
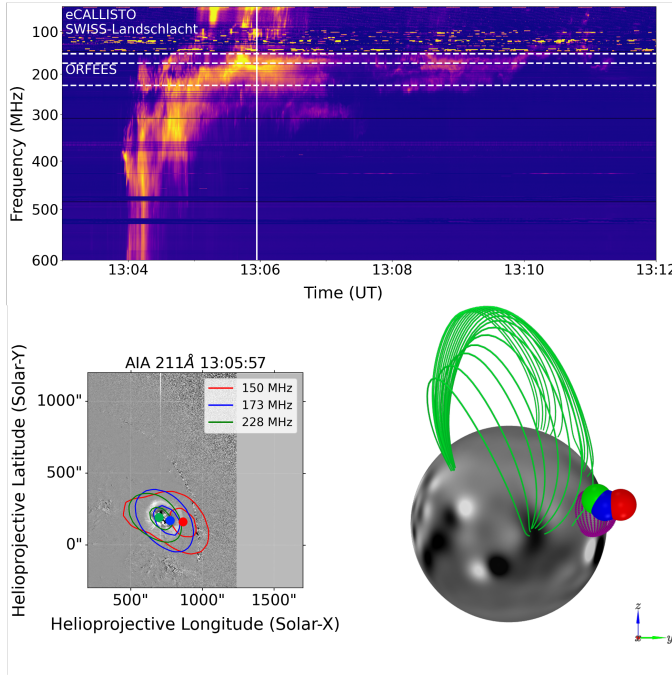


Fig. A.10: Date: 2025/03/11



Appendix B: Shock reconstruction

The shock observations from multiple spacecraft allow us to reconstruct the shock surface using a simple self-similar expanding spheroid. The fitting parameters for the spheroid surface are reported in the Table B.1. The table consists of Heliographic coordinates of the sphere on the solar surface, heliocentric distance (r_c) of the spheroid centre, along with other parameters. The table also consists of self-similar constant (κ) and eccentricity (ϵ) to describe the geometry of the spheroid. The definitions of these fitting parameters can be found in Kouloumvakos et al. (2022).

Table B.1: Spheroid fitting parameters determined using the PyThea tool for the shocks associated with the type II bursts.

Date	Time (UT)	Heliographic longitude	Heliographic latitude	Heliocentric distance r_c (R_\odot)	Radial axis (R_\odot)	Orthogonal axis (R_\odot)	Apex height (R_\odot)	Self similar constant κ	Eccentricity ϵ
2021/06/09	12:03	112.34	26.17	1.13	0.35	0.34	1.48	0.70	0.26
	12:04	112.34	26.17	1.15	0.39	0.38	1.54	0.70	0.26
	12:05	112.34	26.17	1.12	0.49	0.48	1.61	0.78	0.26
	12:06	112.34	26.17	1.13	0.57	0.55	1.70	0.78	0.26
	12:24	112.34	26.17	1.52	1.24	1.20	2.76	0.68	0.26
	12:36	112.34	26.17	1.67	1.60	1.54	3.27	0.68	0.26
	12:48	112.34	26.17	1.83	1.98	1.91	3.81	0.68	0.26
2022/03/28	11:25	13.08	17.75	1.16	0.31	0.33	1.47	0.71	-0.39
	11:27	13.08	17.75	1.21	0.41	0.44	1.62	0.71	-0.39
	11:30	13.08	17.75	1.28	0.53	0.58	1.81	0.71	-0.39
	11:32	13.08	17.75	1.36	0.67	0.73	2.03	0.71	-0.39
	11:37	13.08	17.75	1.48	0.92	0.99	2.40	0.71	-0.39
	12:23	13.08	17.75	2.72	3.26	3.54	5.98	0.71	-0.39
	12:02	120.21	-37.68	1.12	0.19	0.21	1.31	0.68	-0.38
2022/05/19	12:06	120.21	-37.68	1.22	0.43	0.46	1.65	0.71	-0.38
	12:08	120.21	-37.68	1.26	0.49	0.53	1.75	0.71	-0.38
	12:24	120.21	-37.68	1.54	1.02	1.11	2.56	0.71	-0.38
	12:36	120.21	-37.68	1.67	1.29	1.39	2.96	0.71	-0.38
	12:48	120.21	-37.68	1.80	1.54	1.66	3.34	0.71	-0.38
	12:51	51.70	20.87	1.08	0.29	0.29	1.37	0.78	0.00
	12:53	51.70	20.24	1.12	0.35	0.33	1.47	0.71	0.27
2022/11/19	13:00	51.70	20.24	1.19	0.53	0.51	1.72	0.71	0.27
	13:05	51.70	20.24	1.25	0.72	0.69	1.97	0.71	0.27
	13:11	51.70	21.49	1.37	1.03	0.99	2.40	0.71	0.27
	13:21	51.70	21.49	1.45	1.26	1.21	2.71	0.71	0.27
	13:38	51.70	21.49	1.71	2.00	1.92	3.71	0.71	0.27
	12:13	43.92	-4.05	1.12	0.38	0.37	1.5	0.73	0.25
	12:31	44.68	1.28	1.48	1.15	1.12	2.63	0.69	0.22
2024/03/10	12:36	44.68	1.28	1.54	1.31	1.28	2.85	0.69	0.22
	12:41	44.68	1.28	1.60	1.44	1.41	3.04	0.69	0.22
	12:48	44.68	3.19	1.65	1.58	1.54	3.23	0.69	0.22
	13:25	44.68	4.47	1.88	2.12	2.07	4.00	0.69	0.22
	13:36	44.68	4.47	1.95	2.31	2.25	4.26	0.69	0.22
	14:26	-69.62	-16.62	1.20	0.40	0.40	1.60	0.67	-0.18
	14:29	-69.62	-16.62	1.26	0.49	0.50	1.75	0.67	-0.18
2024/05/29	14:31	-69.62	-16.62	1.29	0.56	0.57	1.85	0.67	-0.18
	14:33	-69.62	-16.62	1.34	0.66	0.67	2.00	0.67	-0.18
	14:36	-69.62	-16.62	1.43	0.82	0.84	2.25	0.67	-0.18
	12:08	-28.22	-3.45	1.39	0.43	0.43	1.82	0.53	0.00
	12:11	-28.22	-3.45	1.47	0.53	0.53	2.00	0.53	0.00
2024/11/10	12:12	-28.22	-3.45	1.50	0.57	0.57	2.07	0.53	0.00
	12:14	-28.22	-3.45	1.56	0.63	0.63	2.19	0.53	0.00
	12:15	-28.22	-3.45	1.59	0.66	0.66	2.25	0.53	0.00
	12:21	-28.22	-3.45	1.76	0.85	0.85	2.61	0.53	0.00